



UvA-DARE (Digital Academic Repository)

The effect of stiffened diabetic red blood cells on wall shear stress in a reconstructed 3D microaneurysm

Czaja, B.; de Bouter, J.; Heisler, M.; Závodszy, G.; Karst, S.; Sarunic, M.; Maberley, D.; Hoekstra, A.

DOI

[10.1080/10255842.2022.2034794](https://doi.org/10.1080/10255842.2022.2034794)

Publication date

2022

Document Version

Final published version

Published in

Computer Methods in Biomechanics and Biomedical Engineering

License

CC BY-NC-ND

[Link to publication](#)

Citation for published version (APA):

Czaja, B., de Bouter, J., Heisler, M., Závodszy, G., Karst, S., Sarunic, M., Maberley, D., & Hoekstra, A. (2022). The effect of stiffened diabetic red blood cells on wall shear stress in a reconstructed 3D microaneurysm. *Computer Methods in Biomechanics and Biomedical Engineering*, 25(15), 1691-1709. <https://doi.org/10.1080/10255842.2022.2034794>

General rights

It is not permitted to download or to forward/distribute the text or part of it without the consent of the author(s) and/or copyright holder(s), other than for strictly personal, individual use, unless the work is under an open content license (like Creative Commons).

Disclaimer/Complaints regulations

If you believe that digital publication of certain material infringes any of your rights or (privacy) interests, please let the Library know, stating your reasons. In case of a legitimate complaint, the Library will make the material inaccessible and/or remove it from the website. Please Ask the Library: <https://uba.uva.nl/en/contact>, or a letter to: Library of the University of Amsterdam, Secretariat, Singel 425, 1012 WP Amsterdam, The Netherlands. You will be contacted as soon as possible.

UvA-DARE is a service provided by the library of the University of Amsterdam (<https://dare.uva.nl>)

The effect of stiffened diabetic red blood cells on wall shear stress in a reconstructed 3D microaneurysm

Benjamin Czaja^a, Jonathan de Bouter^a, Morgan Heisler^c, Gábor Závodszy^{a,b}, Sonja Karst^d, Marinko Sarunic^c, David Maberley^e and Alfons Hoekstra^a

^aComputational Science Lab, Faculty of Science, Institute for Informatics, University of Amsterdam, Amsterdam, Netherlands;

^bDepartment of Hydrodynamic Systems, Budapest University of Technology and Economics, Budapest, Hungary; ^cSchool of Engineering Science, Faculty of Applied Sciences, Simon Fraser University, Burnaby, BC, Canada; ^dDepartment of Ophthalmology and Optometry, Medical University Vienna, Vienna, Austria; ^eDepartment of Ophthalmology and Visual Sciences, University of British Columbia, Vancouver, BC, Canada

ABSTRACT

Blood flow within the vasculature of the retina has been found to influence the progression of diabetic retinopathy. In this research cell resolved blood flow simulations are used to study the pulsatile flow of whole blood through a segmented retinal microaneurysm. Images were collected using adaptive optics optical coherence tomography of the retina of a patient with diabetic retinopathy, and a sidewall (sacciform) microaneurysm was segmented from the volumetric data. The original microaneurysm neck width was varied to produce two additional aneurysm geometries in order to probe the influence of neck width on the transport of red blood cells and platelets into the aneurysm. Red blood cell membrane stiffness was also increased to resolve the impact of rigid red blood cells, as a result of diabetes, in blood flow. Wall shear stress and wall shear stress gradients were calculated throughout the aneurysm domains, and the quantification of the influence of the red blood cells is presented. Average wall shear stress and wall shear stress gradients increased due to the increase of red blood cell membrane stiffness. Stiffened red blood cells were also found to induce higher local wall shear stress and wall shear stress gradients as they passed through the leading and draining parental vessels. Stiffened red blood cells were found to penetrate the aneurysm sac more than healthy red blood cells, as well as decreasing the margination of platelets to the vessel walls of the parental vessel, which caused a decrease in platelet penetration into the aneurysm sac.

ARTICLE HISTORY

Received 13 November 2020
Accepted 24 January 2022

KEYWORDS

Red blood cells; diabetic retinopathy; microaneurysm; blood flow; wall shear stress

1. Introduction


Diabetes is characterized by high blood sugar levels or *hyperglycemia* due to insulin resistance or deficiency in the body (Care et al. 2006). Diabetic retinopathy (DR) is diabetes-induced damage to the retina, possibly linked through hyperglycemia (Tarr et al. 2010; Ahsan 2015). It is a common cause of blindness in adults: DR was estimated to be prevalent at 3.4% in the USA (2004), with 0.75% of the general public having vision-threatening DR (Kempen et al. 2004). The International Diabetes Federation estimated worldwide diabetes prevalence at 8.8% in 2015 and predicts 10.4% in 2040 (Ogurtsova et al. 2017).

Diabetic retinopathy is generally classified into two stages of development, earlier *non-proliferative* DR

(NPDR), which is characterized by increased vascular permeability, microaneurysm (MA) formation, and retinal hemorrhages (Wilkinson et al. 2003), and an advanced stage, *proliferative* DR (PDR), where eyes exhibit the growth of new blood vessels (neovascularization) and may develop vitreous or preretinal hemorrhaging (Wilkinson et al. 2003), which causes macular edema and retinal thickening (Engerman 1996; Ciulla et al. 2003; Williams et al. 2004; Fong et al. 2007). Retinal MAs are considered a hallmark of DR (Dubow et al. 2014), and are one of the early indicators noted in presymptomatic DR screening (Faust et al. 2012).

Hemodynamic changes have been found to influence the progression of proliferative DR (Klein and Klein 2002; Hennis et al. 2003; Tarr et al. 2010).

CONTACT Benjamin Czaja  B.E.Czaja@uva.nl, benjamin.czaja@gmail.com

 Supplemental data for this article is available online at <https://doi.org/10.1080/10255842.2022.2034794>.

© 2022 The Author(s). Published by Informa UK Limited, trading as Taylor & Francis Group
This is an Open Access article distributed under the terms of the Creative Commons Attribution-NonCommercial-NoDerivatives License (<http://creativecommons.org/licenses/by-nc-nd/4.0/>), which permits non-commercial re-use, distribution, and reproduction in any medium, provided the original work is properly cited, and is not altered, transformed, or built upon in any way.

Specifically, elevated levels of vascular endothelial growth factor (VEGF) have been connected with diabetic retinopathy (Adamis et al. 1994; Caldwell et al. 2003) by inducing vessel permeability (Mathews et al. 1997) and the formation of new blood vessels (Aiello et al. 1995b; Hoeben et al. 2004). The pathophysiology of DR includes the thickening of the vascular basement membrane (Roy et al. 2010) which affects oxygen transport to the retina and leads to secondary VEGF production, which has been found to be induced in response to tissue hypoperfusion (hypoxia/ischemia) (Aiello et al. 1994, 1995a; Gupta et al. 2013). Expression of VEGF by the endothelial cells has also been found to be stimulated by hemodynamic shear stresses on the vessel wall (Ballermann et al. 1998; Shay-Salit et al. 2002; Dela Paz et al. 2012), especially the increase of wall shear stress (WSS) has been identified to cause endothelial dysfunction (Kohner 1993). Studying the influence of whole blood flow on WSS patterns in the retinal micro-vasculature may help the understanding of the increased amounts of VEGF in diabetic retinopathy.

Computational fluid dynamic (CFD) studies focusing on aneurysms, particularly cerebral aneurysms (CA), is a well established field (Sforza et al. 2009). Such studies have uncovered novel metrics for identifying high-risk CAs (Sforza et al. 2012) such as size (Bhagal et al. 2018), as well as the ratio of aneurysm height to neck-diameter in sacciform type aneurysms (Ujiie et al. 2001; Meng et al. 2014). However, CFD applied to retinal microaneurysms is still developing in comparison. Studies have been applying CFD to the vascular network in the diabetic eye (Lu et al. 2016), with recent work proposing morphology and CFD estimation of perfusion parameters to be useful indicators for determining the likelihood of clot presence in individual diabetic MAs (Bernabeu et al. 2018; Sampani et al. 2018). Other work has associated the MA-to-vessel radius ratio as a potential marker for assessing risk of MA leakage (Ezra et al. 2013).

To the best of our knowledge, all numerical studies performed in MAs have assumed blood to be a continuous fluid (Ezra et al. 2013; Lu et al. 2016; Bernabeu et al. 2018), likely due to the complexity and computational cost of using cell-based blood flow models. There have been cell-resolved blood flow simulations conducted in 2D, with comparatively lower computational overhead, in aneurysm-like geometries (Mountrakis et al. 2013; Czaja et al. 2018), but never in patient specific aneurysms. Some recent three dimensional cell resolved numerical work was carried estimating the wall shear stress and gradients in wall shear stress patterns in

micro-vascular vessel networks (Balogh and Bagchi 2019), and should serve as precedence for this study. MAs present an incredibly interesting environment to employ cell-resolved blood flow models, as these are the scales at which the non-Newtonian behavior of whole blood is most evident (Pries et al. 1994; Bagchi 2007), primarily the Fåhræus–Lindqvist effect (Fåhræus and Lindqvist 1931). Continuum flow simulations have also been found incapable to accurately represent shear rates, shear stresses, and therefore WSS (Rooij et al. 2019). Furthermore, contemporary imaging technologies such as intravenous fluorescein angiography and optical coherence tomography angiography (OCTA) exhibit differences when visualizing MAs. OCTA for example, captures cellular movement within the vessels, and therefore might not exhibit a signal in the absence of cellular flow within the aneurysms. We believe that cell resolved simulations can help understand this differential between imaging techniques while probing the cellular flow environment in such MAs.

In this study, we present 3D cell-resolved blood flow simulations in a sacciform retinal microaneurysm geometry. The geometry was segmented from Adaptive Optics Optical Coherence Tomography (AO-OCT) images of the retina of a patient with DR. To our knowledge, this is the first study to simulate cell-resolved blood flow in an MA geometry. Additionally pulsatile flow was considered for the computing of wall shear stress, wall shear stress gradients, and cell transportation presented in this study. First we present the segmentation of the MA geometry, and a modification of the original geometry to produce two additional geometries to probe cell perfusion due to changes in aneurysm neck width. We present the computed WSS patterns in the microaneurysm, highlighting the influence of red blood cells (RBCs), and the influence of RBC rigidity. The transport and the sensitivity of the penetration depth of red blood cell and platelets into the aneurysmal sac are also presented.

2. Materials and methods

2.1. AO-OCT image acquisition

Adaptive Optics combined with Optical Coherence Tomography (AO-OCT) is a tomographical (i.e. slice-by-slice) imaging technique which directs a low-coherence light beam into, in this case, the retina of the eye, measuring all light (and interference) that scatters back from a specific depth. Images were obtained using the swept source prototype OCT system of Ju et al. (2017), with a center wavelength of 1.06 μm and a 200 kHz sweep rate (Axsun Technology

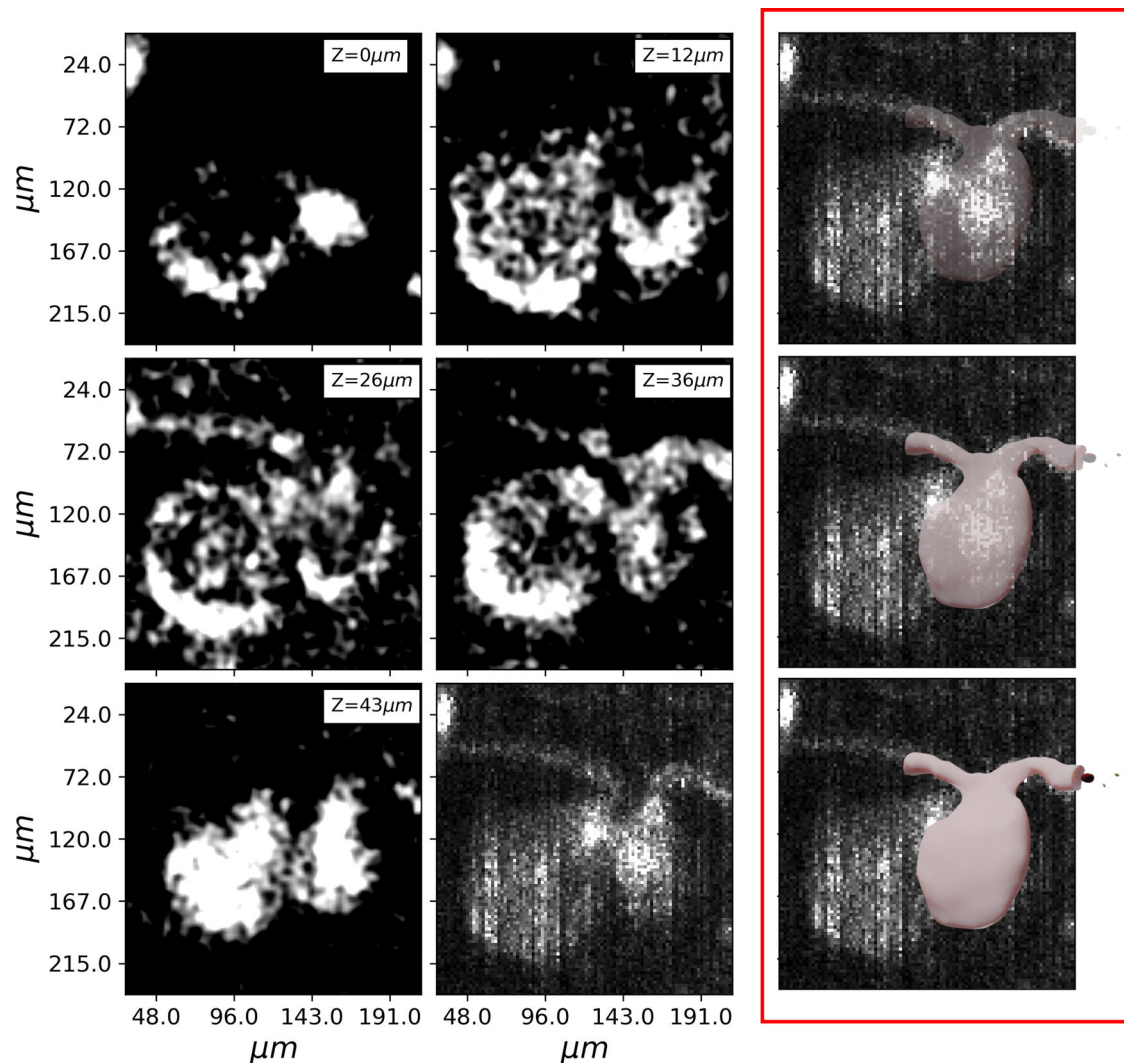


Figure 1. AO-OCT images of a sidewall sacciform retinal microaneurysm at different depths. The five panels of the first two columns, starting from the top left and progressing to the bottom left, show the microaneurysm per depth. The bottom middle panel shows the final stacked image, highlighting the overall 2D side view of the MA. The MA used for this study was only the smaller, right, lobe of the MA. The segmented smoothed MA geometry is overlaid onto the final raw AO-OCT image in the right column, which is outlined in red.

Inc.). The axial resolution defined by the -6 dB width was measured to be $8.5 \mu\text{m}$ in air (corresponding to a resolution of $6.2 \mu\text{m}$ in tissue ($n=1.38$)), and the transverse resolution with a 5.18 mm beam diameter incident on the cornea was estimated to be $3.6 \mu\text{m}$ assuming a 22.2 mm focal length of the eye and refractive index of 1.33 for water at $1.06 \mu\text{m}$ (Heisler et al. 2018). The retina was sampled in a 400×400 grid of A-scans (i.e. depth-wise scans), which were combined to produce the volumetric data set. Each B-scan location was imaged four times in order to produce the angiographic image by calculating the OCT signal variance across each set of repeated scans within the volume. A spatial resolution of $\approx 3 \mu\text{m}$ was achieved (Ju et al. 2017) with a $450 \times 450 \mu\text{m}$ field of view. Figure 1 displays a sub-region of the AO-OCT

data, focusing on the microaneurysm used in this study. OCTA data was also provided as a reference in the segmentation of the AO-OCT data. Videos comparing the two data sets side-by-side are presented in the [supplementary material](#).

2.2. Model segmentation

MAs are categorized into six morphologies; saccular/sacciform, focal bulge, fusiform, mixed, irregular, and pedunculated (Moore et al. 1999; Lombardo et al. 2013; Dubow et al. 2014), with saccular/sacciform being the most common (Dubow et al. 2014). Consistent with literature, we define Aspect Ratio as the ratio of the height of the sac h (entrance to bottom) to the perpendicular aneurysm neck diameter

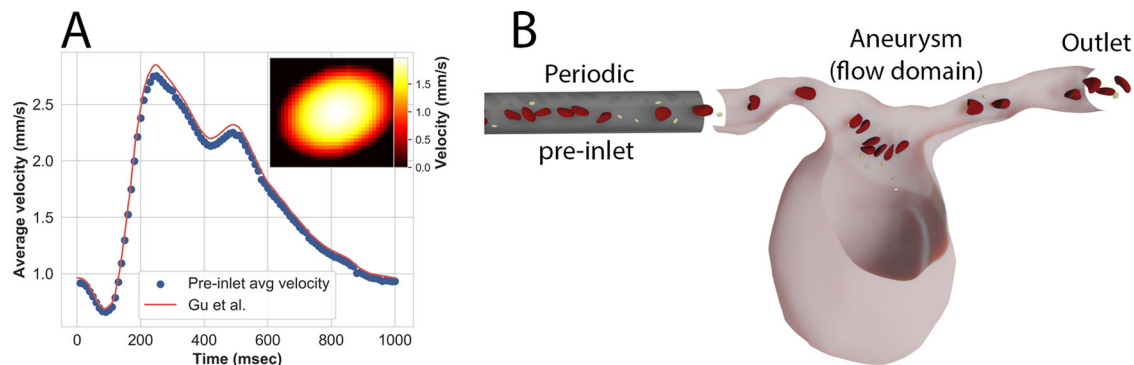


Figure 2. Driving force and Boundary conditions. (A) The time-dependent velocity in the pulsatile simulations matches erythrocyte velocity measurements averaged over multiple retinal capillaries and cardiac cycles (Gu et al. 2018). The heat map depicts pre-inlet plasma velocity over an averaged cross-section. Note that the cross-section is not fully circular. (B) Inflow boundary conditions in the aneurysm geometry are copied from a periodic pre-inlet domain to the flow domain. RBCs and platelets are depicted in red and white respectively.

n_d , $AR = h/n_d$. The final segmented MA geometry from the AO-OCT data is a sidewall sacciform aneurysm with an AR of approximately 2.8. Multiple depth slices are shown in Figure 1, with a final stacked image in the bottom right panel. Smaller aneurysms in the images were close in size to the image voxel size, proving difficult to distinguish vessel contours and limiting segmentation. Therefore, the microaneurysm that was chosen for segmentation was comparatively larger than the others in the image. The authors estimate that the MA considered in this study is in the upper 10% of MAs based on size (Dubow et al. 2014; Karst et al. 2018; Lammer et al. 2018). The identified microaneurysm exhibited an irregular multi-lobed shape as no parental vessel pairs could be distinctly resolved to determine two separate aneurysms. In order to study the blood flow in a common sidewall aneurysm morphology, only the smaller lobe of the seemingly irregular aneurysm, shown in Figure 1 was segmented. The final segmented aneurysm geometry, Figure 2(B) is a representative common type sacciform aneurysm.

A median filter with window size 3 (i.e. a $3 \times 3 \times 3$ Moore neighborhood) was applied to the volumetric AO-OCT data to reduce noise. Segmentation was carried out with ITK-SNAP using the marching cubes algorithm. The feeding and draining vessels were assumed to be approximately radially symmetric and smooth, with small irregularities due to image noise. The resulting segmented geometry was further smoothed via Laplacian smoothing in MeshLab, and is presented in the right panel of Figure 2. The final resulting vessel mesh consists of approximately 67,000 vertices, which corresponds to a resolution of approximately one tenth of a micron or below per triangular surface element.

The neck diameter n_d of this model was modified to produce two additional geometries with ARs of approximately 1.7 and 3.7. It should be noted that the nomenclature of AR in this study is used as a matter of labelling to stay consistent with previous studies (de Sousa et al. 2016). Changes made to the sac size would produce markedly different aneurysm geometries as well as flow conditions while still be reported by the same AR. Varying the neck width in this study was carried out to probe cell perfusion in the aneurysm domains. The original geometry neck width was modified to create the smaller and larger aneurysm necks respectively while the parental vessel diameters were kept the same. However the leading vessel of the AR 1.7 geometry was widened in order to alleviate a non-physical step like vessel increase from feeding vessel to aneurysm sac. The different geometries are referred by their aspect ratio AR 1.7, AR 2.8 (original) and AR 3.7. All relevant dimensions of the microaneurysms are listed in Table 1. The average diameters of the feeding vessel and draining vessel were estimated by averaging over four different diameter measurements.

2.3. Hemocell and computational resources

Cell resolved blood flow simulations have made significant progress in recent years. These numerical models are generally built upon continuous CFD solvers with a mechanical model describing the membrane properties of a RBC. Methods vary from particle based methods fluid solvers (Noguchi and Gompper 2005; McWhirter et al. 2009; Fedosov et al. 2010), to mesoscale lattice based methods (Melchionna et al. 2010; Kotsalos et al. 2019). The numerical blood flow simulations are carried out, in

Table 1. Dimensions of microaneurysm geometries.

	Diameter		
	Max.	Avg.	Min.
Feeding vessel	21 μm	15 μm	9 μm
Draining vessel	21 μm	16 μm	9 μm
AR 1.7 neck	71 μm	57 μm	30 μm
AR 2.8 neck	44 μm	36 μm	21 μm
AR 3.7 neck	33 μm	27 μm	16 μm
Parental vessel length		204 μm	
Parental vessel volume		$33 \cdot 10^3 \mu\text{m}^3$	
Aneurysm dome height		99 μm	
Aneurysm volume		$222 \cdot 10^3 \mu\text{m}^3$	

this study, with the open-source cell resolved blood flow solver HemoCell. HemoCell is a high-performance framework for dense cellular suspension flows which models the plasma with the Lattice Boltzmann method and the mechanical model for the suspended RBCs are modeled with a discrete element model which are connected to the plasma via the immersed boundary method (Závodszy et al. 2017, 2019; Rooij et al. 2019; Czaja et al. 2020). The finite element force model for the RBC membrane is a superposition of four discrete forces acting on a single triangle element of the cellular membrane. The link force (F_{link}) models the stretching and compression of the underlying spectrin-network, the bending force (F_{bend}) models the bending response of the membrane arising from the non-zero thickness of the spectrin-network, the area force (F_{area}) models the combined surface response of the supporting spectrin-network and the lipid bilayer of the membrane to stretching and compression, and the volume force (F_{volume}) maintains the quasi-incompressibility of the cell. The model additionally incorporates a 5:1 viscosity contrast between cytosol and blood plasma (De Haan et al. 2018). The surface Young modulus of the RBC model was computed to be $E_s = 27.82 \mu\text{N/m}$ (Závodszy et al. 2017) which is inside the expected range of 25–50 $\mu\text{N/m}$ (Maciaszek and Lykotrafitis 2011). Additionally the compression modulus was computed to be $K = 21.88 \mu\text{N/m}$, which is agreement with the range found in a cellular micro-rheology study (Park et al. 2011). The bending modulus was computed to be 80 k_{BT} which is in agreement with the order or magnitude of 50 k_{BT} proposed by micropipet aspiration tests (Evans 1983). The RBCs have a diameter of $\approx 8 \mu\text{m}$ with a volume of 97.6 μm^3 which is in the range of 80–100 μm^3 (Maner and Moosavi 2019). Platelets which are much smaller than RBCs, typically 1–2 μm in diameter, are modelled as rigid discoids and are governed by the same finite element model as the RBCs but with each force scaled up by a factor of 10. This produces at least an order of magnitude stronger platelet membrane responses for small deformations

than the response of RBCs, which is inline with recent observations (Haga et al. 1998). The kinematic viscosity of the suspending blood plasma was set to $\eta = 1.1e^{-6} \text{ m}^2/\text{s}$.

The HemoCell model has been validated to reproduce the hallmark individual RBC mechanics, as well as the non-Newtonian bulk flow properties (Závodszy et al. 2017). It has been further developed to model the stiffening of RBCs due to oxidative stress (Czaja et al. 2020; de Vries et al. 2020), and has recently been applied to study platelet margination (Závodszy et al. 2019) and aggregation (Rooij et al. 2019). The full details and validation of the HemoCell blood flow solver is out of the scope of this present research, and the authors invite the reader to www.hemocell.eu for complete model publications and code support.

The blood flow simulations (15 in total) were executed on the Cartesius and Lisa clusters at SURF-sara in Amsterdam, the Netherlands. Each simulation was distributed over 45 compute cores, and each simulation took approximately fifteen days walltime to achieve a simulated physical second. The spatial scale of the lattice was set to $dx = 0.5e^{-6} \text{ m}$ with a time-step of $dt = 1e^{-7} \text{ s}$.

2.4. Boundary conditions

Given the anti-symmetric nature of the MA, cells can become trapped, leading to a nonphysical depletion of cells in the parental vessel when using periodic boundary conditions. Also the size and shape of the inlet and outlet may differ, making it unfeasible to join the outlet and inlet in periodic boundary conditions. For this reason the inflow and outflow boundary conditions of (Azizi Tarksalooyeh et al. 2018) are employed and extended to 3D in this study. Inflow is regulated with the use of a periodic *pre-inlet* domain that is (one-way) coupled to the aneurysm domain providing velocity as inlet boundary condition. Due to the periodicity of the pre-inlet, the upstream flow profile has sufficiently equilibrated when it is introduced to the flow domain. The outflow boundary in the aneurysm geometry is kept at a constant pressure, which induces a pressure difference that is built up over the flow domain. To ensure no transient flow is introduced into the aneurysm domain by the inlet and outlet, the inlet and outlet is placed sufficiently far enough away to not affect the flow domain. Due to the low Reynolds numbers present on the micro-capillary scale ($Re < 0.5$ (Hoskins and Hardman 2017)), a relatively short distance is required to

develop an equilibrium flow profile. Following the relationship $L_e = 0.035D \cdot Re$ (Bird et al. 2007) which relates the length L_e that a prescribed velocity profile at an inlet will recover to its theoretical flow profile given the vessel diameter D and Reynolds number Re . The inflow region and outflow region were placed approximately 24 and 18 μm away from the entrance of the aneurysm sac respectively. Additionally the length L_c of a vessel required for the full development of cell-free layer has been identified to be $L_c \leq 25D$ for radially symmetric vessel sizes under steady state flowing conditions to be in the range of $10 \leq D \leq 100 \mu\text{m}$ (Katanov et al. 2015). This suggests that cells in the pre-inlet will need to travel approximate maximum length of 375 μm , which corresponds to about 1.5 laps in the pre-inlet. We anticipate that this will have a negligible start up effect in the scope of the full simulation. The final segmented model is depicted in Figure 2(B), including boundary conditions.

RBCs and platelets are initialized in the pre-inlet an approximate tube hematocrit of 3.7% and a platelet-to-RBC-ratio of 1/10. It is documented that the actual hematocrit in the microcirculation is much less than the systemic hematocrit, which has been measured to be 8–10% on average in the microcirculation when the systemic hematocrit is reported at 35–40% (Johnson 1971; Lipowsky et al. 1978; Klitzman and Duling 1979). Additionally the hematocrit in the microcirculation can vary 6–10% between micro vessels (Lipowsky et al. 1978). Initializing hematocrits up to and above 10% in such small vessels without introducing un-physical spatial structure of cells is far from trivial. The force-bias model (Bargieł and Mościński 1991) of enclosing ellipsoids was applied to initialize a random hematocrit distribution that insured numerical stability for the entire run time of the simulations. We believe that the cell initializations in this study are lower than the expected physiological hematocrit but represents the current state of the art of such cell resolved blood flow models applied over such long timescales.

2.5. Initial conditions

2.5.1. Steady and pulsatile flow

The velocity of the feeding vessel was matched to velocities of human retinal capillaries, of similar sizes, measured via rapid high resolution imaging with a dual-channel scanning technique (de Castro et al. 2016). This was achieved by driving the simulation via a body force applied to the pre-inlet domain, which resulted in a mean velocity of 1.69 mm/s across

the pre-inlet, with a maximum velocity of 3.52 mm/s in the center of the vessel. It should be noted that due to the patient-specific geometry, which is not radially symmetric, this resulted in an offset from the theoretical Hagen–Poiseuille profile. Figure 2(A) depicts a velocity heat map of the blood plasma, for the averaged cross-section of the pre-inlet, which reached equilibrium within 0.001 second of simulation startup.

For pulsatile simulations we match the waveform of the time-dependent driving force to erythrocyte velocity measurements averaged over multiple retinal capillaries and cardiac cycles (Gu et al. 2018), as depicted in Figure 2(A). The associated Reynolds numbers range between 0.022 and 0.092. We modified the waveform such that it starts and ends with the same velocity value, wrapping around periodically to the same value at the beginning and end of the waveform.

2.5.2. Stiffened red blood cells

It is known that due to the increased reactive oxygen species present in diabetes, red blood cells undergo oxidative stress (Giugliano et al. 1996), resulting in reduced RBC deformability (Garnier et al. 1990; Tsukada et al. 2001; Shin et al. 2007; Agrawal et al. 2016). Oxidative stress primarily impacts the cytoskeletal network of the RBC (Caprari et al. 1995), which we numerically model with a network of links following a worm-like-chain potential (Závodszy et al. 2017). A stiffened HemoCell RBC model has recently been developed to model the stiffened an RBC membrane undergoes during oxidative stress (Czaja et al. 2020; de Vries et al. 2020). Specifically this is achieved by increasing the link force coefficient to a value of $F_{link} = 140 k_B T$, which results in an increased surface elastic modulus of $378.32 \frac{\mu\text{N}}{\text{m}}$ compared to the healthy RBC modulus of $27.82 \frac{\mu\text{N}}{\text{m}}$ (Závodszy et al. 2017). This increase in cell stiffness falls within the range previously found for a diabetes induced stiffened RBCs (Chang et al. 2017).

3. Results

3.1. Wall shear stress

The benefit of using Lattice Boltzmann as the underlying fluid solver is that the viscous stress tensor can be easily recovered from the lattice

$$\sigma_{x,y,z} = - \left(1 - \frac{\delta t}{2\tau} \right) \Pi_{x,y,z}^{(1)} \quad (1)$$

where δt is the timestep, τ is the relaxation time, and $\Pi_{x,y,z}^{(1)}$ is the perturbation momentum calculated

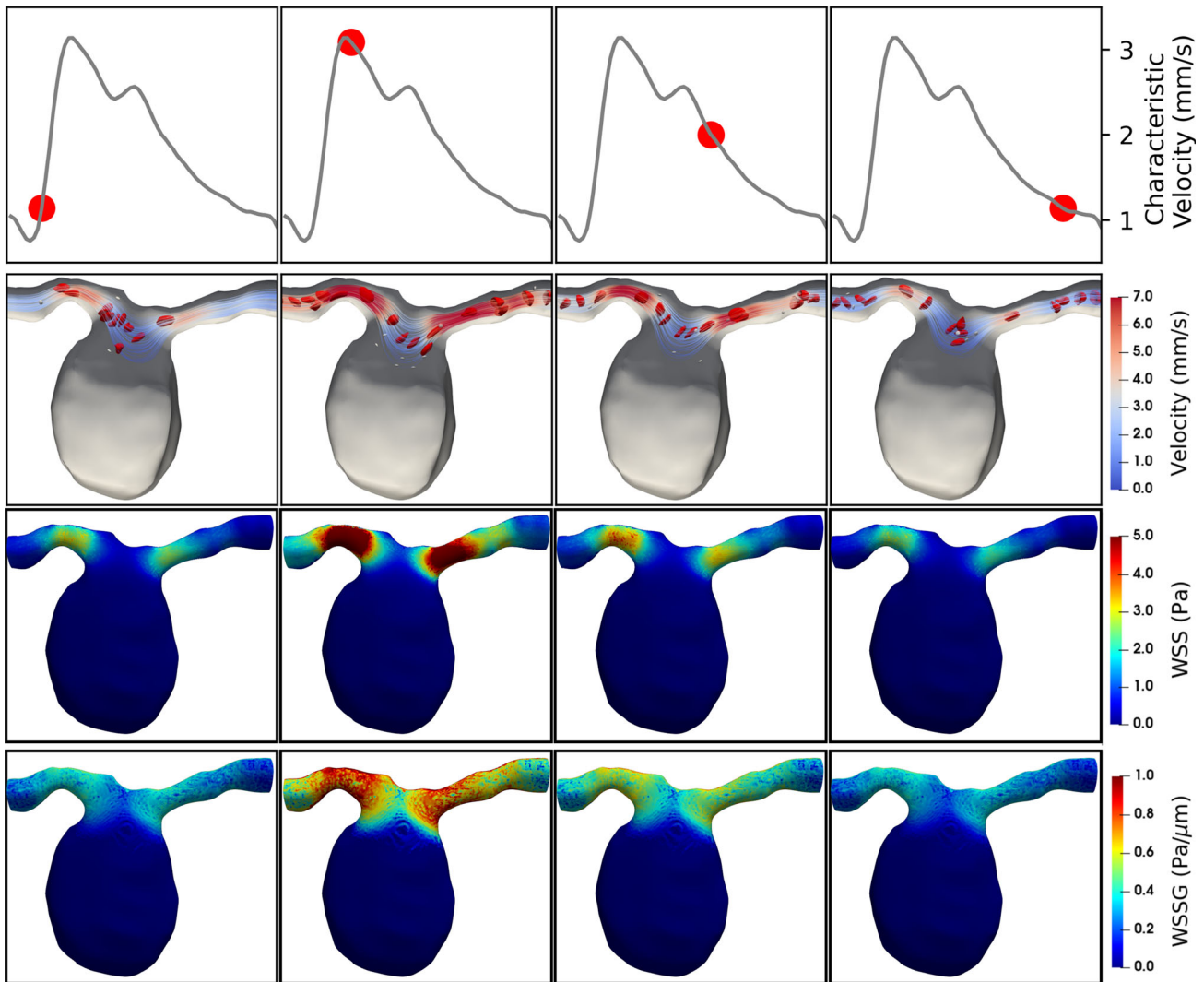


Figure 3. Characteristic flow velocity, WSS, and WSS gradients in the original AR 2.8 geometry during a full heartbeat. Parental vessel characteristic velocity (first row), velocity streamlines (second row), WSS (third row), WSSG magnitude (fourth row).

following (Timm et al. 2016). Wall shear stress is then the force per unit area exerted on the vessel wall in the direction that is tangent to the local vessel wall normal (Krüger et al. 2009; Stahl et al. 2010).

$$\tau = \sigma \cdot n \quad (2)$$

In practice WSS is the normal component of the viscous stress vector at the wall which is obtained by calculating the dot product of the stress tensor from the lattice Boltzmann fluid field with the surface normal vector of the vessel mesh using the visualization application ParaView version 3.10, Kitware. The orientation of the normals of the MA vessel wall is computed from the final segmented geometry, shown in the right panel of Figure 2. The wall shear stress gradient (WSSG) is computed by taking the spatial gradient of the WSS vector. In practice this is calculated by taking the local gradient of WSS at each triangle face of the vessel mesh. The local gradient at

each triangle face is the average of the spatial gradients of its component vertices in order to mitigate discontinuities in the mesh. Only the magnitude of WSS and WSSG is reported in this study. Both WSS and WSSG were computed in three specific locations throughout the micro vessel; the feeding vessel, the aneurysm sac, and the draining vessel. The resulting WSS and WSSG patterns in the original (AR 2.8) geometry over a single pulse are shown in Figure 3. The second row shows the major streamlines with the suspended red blood cells, the third row shows the magnitude of the WSS. The spatial mean and standard deviation of WSS and WSSG in each location for each geometry over the course of a heart beat are reported in Tables 2 and 3.

Pulsatile flow induced a change in WSS of approximately 3 Pa over the course of a heart beat. In the case of the original (AR 2.8) geometry WSS in the feeding vessel is observed to increase from 0.9 ± 0.5 Pa at pulse minimum to 3.9 ± 2.2 Pa at pulse maximum.

Table 2. Wall shear stress in MA during a heart beat.

Geometry	Pulse max WSS (Pa)	Pulse min WSS (Pa)	Pulse mean WSS (Pa)	Plasma-only mean WSS (Pa)
Feeding vessel				
AR 1.7	0.3 ± 0.3	0.08 ± 0.06	0.19 ± 0.17	0.3 ± 0.4
AR 2.8	3.9 ± 2.2	0.9 ± 0.5	2.2 ± 1.7	1.3 ± 1.8
AR 3.7	4.1 ± 2.6	1.0 ± 0.5	2.3 ± 1.7	1.3 ± 1.8
Draining vessel				
AR 1.7	1.7 ± 1.2	0.4 ± 0.3	1.04 ± 0.83	0.2 ± 0.3
AR 2.8	2.3 ± 1.5	0.5 ± 0.4	1.33 ± 1.1	0.3 ± 0.4
AR 3.7	2.7 ± 1.8	0.7 ± 0.4	1.61 ± 1.3	0.2 ± 0.4
Aneurysm sac				
AR 1.7	$(3.5 \pm 6.6) \cdot 10^{-3}$	$(1.0 \pm 2.0) \cdot 10^{-3}$	$(2.2 \pm 3.7) \cdot 10^{-3}$	$(3.6 \pm 4.0) \cdot 10^{-3}$
AR 2.8	$(1.1 \pm 1.1) \cdot 10^{-3}$	$(3.3 \pm 5.0) \cdot 10^{-4}$	$(6.3 \pm 8.0) \cdot 10^{-4}$	$(9.6 \pm 5.0) \cdot 10^{-4}$
AR 3.7	$(5.3 \pm 3.7) \cdot 10^{-4}$	$(1.1 \pm 1.0) \cdot 10^{-4}$	$(4.5 \pm 5.3) \cdot 10^{-4}$	$(1.6 \pm 5.0) \cdot 10^{-4}$

Table 3. Wall shear stress gradient in MA during a heart beat.

Geometry	Pulse max WSSG (Pa/μm)	Pulse min WSSG (Pa/μm)	Pulse mean WSSG (Pa/μm)
Feeding vessel			
AR 1.7	0.09 ± 0.11	0.02 ± 0.03	0.05 ± 0.07
AR 2.8	0.83 ± 0.64	0.20 ± 0.15	0.48 ± 0.44
AR 3.7	0.86 ± 0.63	0.21 ± 0.15	0.49 ± 0.44
Draining vessel			
AR 1.7	0.35 ± 0.33	0.08 ± 0.08	0.21 ± 0.23
AR 2.8	0.47 ± 0.34	0.11 ± 0.08	0.28 ± 0.25
AR 3.7	0.62 ± 0.51	0.15 ± 0.13	0.38 ± 0.38
Aneurysm sac			
AR 1.7	$(5.1 \pm 10.0) \cdot 10^{-4}$	$(1.5 \pm 2.7) \cdot 10^{-4}$	$(3.1 \pm 6.6) \cdot 10^{-4}$
AR 2.8	$(1.4 \pm 2.4) \cdot 10^{-4}$	$(4.1 \pm 8.8) \cdot 10^{-5}$	$(8.1 \pm 15.7) \cdot 10^{-5}$
AR 3.7	$(5.5 \pm 5.1) \cdot 10^{-5}$	$(1.4 \pm 2.9) \cdot 10^{-5}$	$(5.3 \pm 8.8) \cdot 10^{-5}$

The standard deviation highlights the spatial distribution of WSS values over the feeding vessel. Pulsatile WSS and WSSG in the other geometries are reported in Tables 2 and 3. Spatial mean WSS and WSSG in the feeding vessel, draining vessel, and aneurysm sac are shown over a full pulse in the top two panels of Figure 4. The spatial mean in each location is shown as a line, and the 95% confidence interval of the mean is shown as a shaded region around the mean.

The influence of geometry on WSS was also considered and is reported via the spatial-temporal mean of WSS. WSS in the original geometry, AR 2.8, was observed to be approximately four orders of magnitude greater in the feeding (2.2 Pa) and draining vessels (1.3 Pa) as compared to the aneurysmal sac ($6.3 \cdot 10^{-4}$ Pa). This drop in WSS from the parental vessel to the aneurysm sac is consistent with a previous CFD estimations (Bernabeu et al. 2018). The feeding vessel which is slightly narrower, exhibited higher WSS values compare to the slightly wider draining vessel. The change in WSS with change in vessel diameter is also consistent with previous cell resolved simulation predictions in vessels with similar diameters (Balogh and Bagchi 2019).

In order to probe the effect neck width on cell transportation the aneurysm neck was enlarged and reduced to produce two additional geometries (AR

1.7 and AR 3.7). The diameter of the feeding vessel in large neck (AR 1.7) case was additionally modified in order alleviate an unrealistic ‘step-like’ transition from parental vessel to sac. The feeding vessel of AR 1.7, therefore exhibited the lowest spatial-temporal mean WSS values (0.19 Pa), with AR 2.8 exhibited an increase (2.22 Pa), and AR 3.8 exhibited the highest WSS values (2.33 Pa). The increase in WSS in the parental vessels of AR 3.7 is attributed to a smaller aneurysm neck width rather than a change in diameter of the parental vessels. As neck width decreased flow inside the aneurysm sac decreased, which resulted in a decrease in WSS in the aneurysm sac as neck width increased. The effects of neck width and vessel diameter are reported here in terms of spatial-temporal mean of WSS in order to highlight geometric effects. Geometric effects on WSS are present over the entire heart beat and show most differences during pulse maximum, which is highlighted in the top left panel of Figure 4.

WSS in the aneurysm sac, however, exhibits a decrease in WSS as neck width decreases. This is a direct result from larger amounts of fluid flow present inside the aneurysmal sac with larger aneurysm neck widths. The computed spatial-temporal mean WSS is 2.2×10^{-3} Pa in the AR 1.7 geometry and decrease to 6.3×10^{-4} Pa in the AR 2.8, and to 4.5×10^{-4} Pa in the AR 3.7 geometry. The plasma velocity streamlines, computed using a Runge–Kutta–Fehlberg integration, show that the major streamlines of the parental vessel do not significantly penetrate the aneurysmal sac. Streamlines penetrate the aneurysm sac less as neck width decreases. WSS patterns follow this trend. The streamlines and resulting WSS patterns over multiple neck widths are shown in a supplementary figure.

Additionally, plasma-only simulations were carried out in each of the geometries to highlight the difference between computing WSS with a continuous method and a cell based method. The pre-inlet of each of the non-pulsatile plasma-only simulations were matched to the temporal mean characteristic

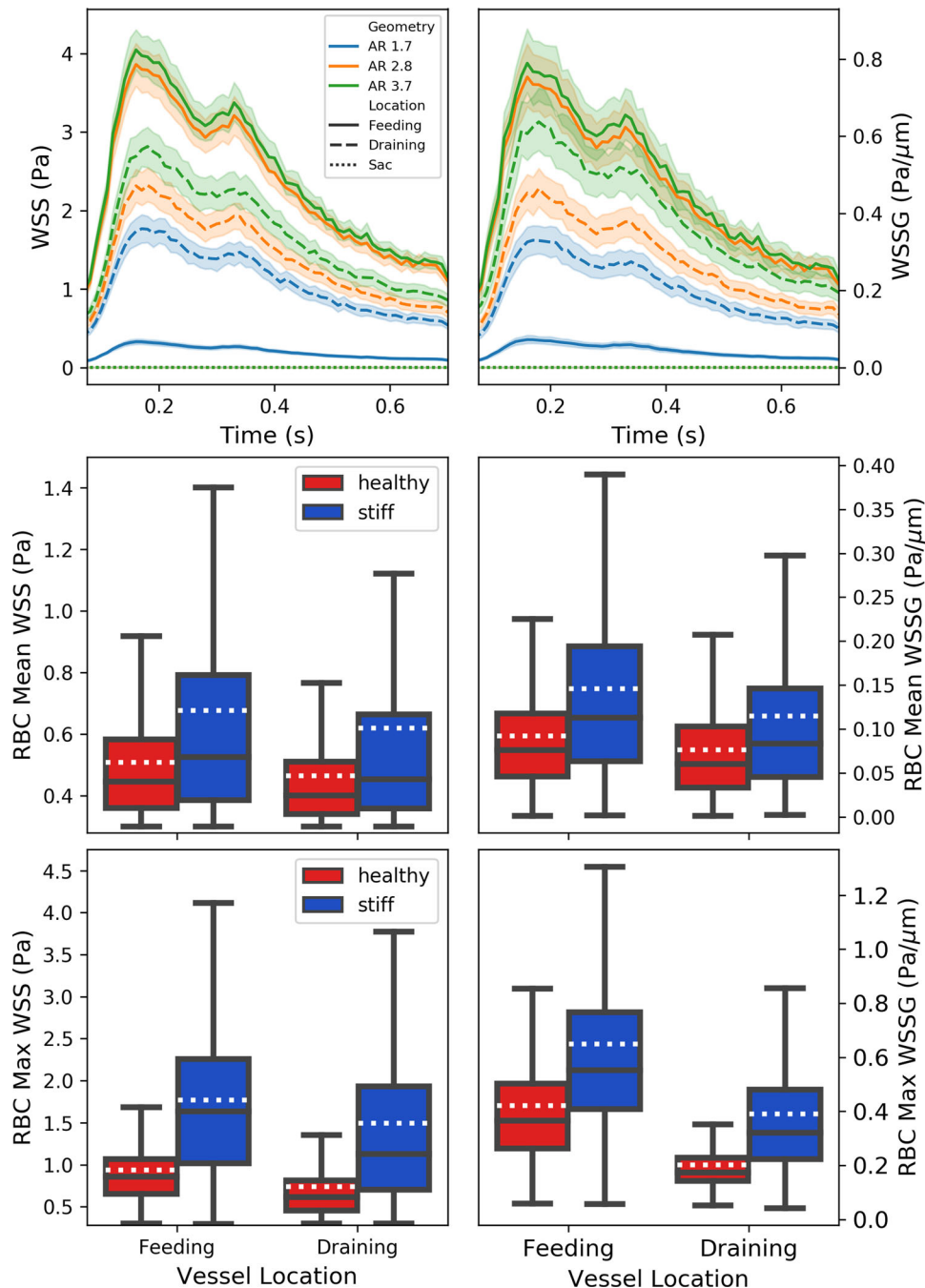


Figure 4. (Top row) Mean WSS and WSSG in feeding vessel, draining vessel, and the aneurysmal sac for all three neck widths. Shaded region around each line highlight the 95% confidence interval of the mean. (Middle row) Distribution of the RBC induced WSS and WSSG spatial-temporal mean in feeding and draining vessels in the AR 2.8 geometry. (Bottom row) Distribution of the spatial-temporal mean of the maximum RBC induced WSS and WSSG signals per cell passing event in feeding and draining vessels in the AR 2.8 geometry. The width of the boxes shows the quartiles of the WSS and WSSG values, while the whiskers extend to include 99% of the computed WSS and WSSG values. RBC induced WSS and WSSG in the aneurysmal sac is not reported due to the lack of cells coming in contact with aneurysmal wall.

velocities of the cell based simulations. The computed WSS in each geometry is reported in Table 2. The WSS in the original AR 2.8 was computed to be 1.3 ± 1.8 Pa in the feeding vessel, 0.3 ± 0.4 Pa in the draining vessel, and $(9.6 \pm 5.0) \times 10^{-4}$ Pa in the aneurysm sac. The computed WSS is markedly lower

in the plasma-only cases as compared to the cell resolved (temporal mean) cases. This decrease of computed WSS when using plasma-only simulations is in agreement with the simulations in the microvasculature network models of (Balogh and Bagchi 2019). It should be noted that a direct comparison

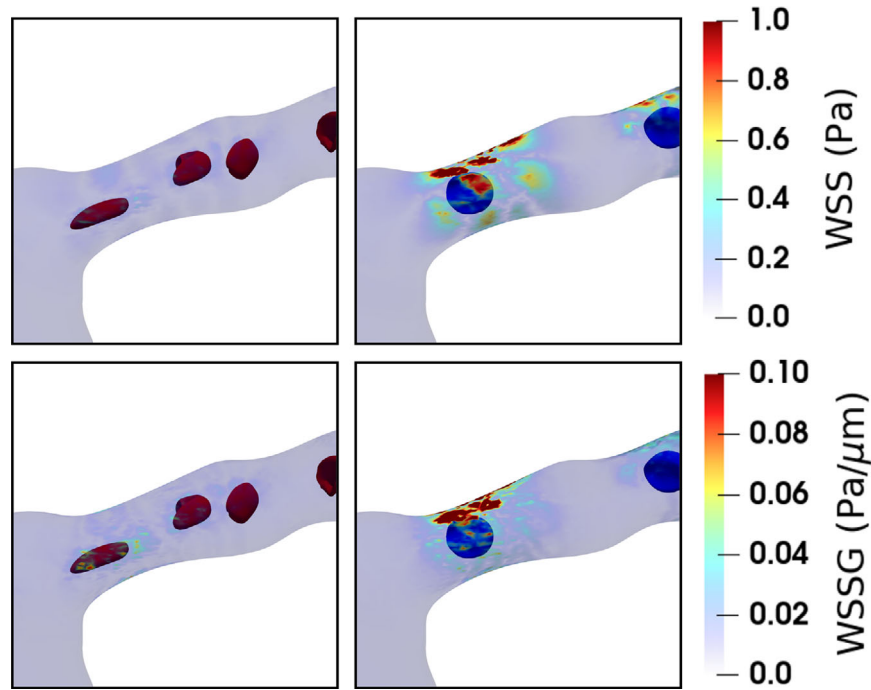


Figure 5. WSS and WSSG patterns induced by passing RBCs. The RBC induced WSS patterns at a time point when a single for healthy (left) and stiff (right) RBC passes through the draining vessel of the original AR 2.8 geometry.

cannot be drawn between the two types of methods, but it should be highlighted that cell resolution allows us to uncover the effect of the size ratio between the RBC and the vessel wall. These simulations should serve as an example highlighting the differences between the two methods when applied in a microvascular geometry.

The spatial wall shear stress gradient (WSSG) was also calculated throughout each simulation and was identified to follow the same trends as WSS. The magnitude of WSSG in the feeding vessel of AR 2.8 was observed to change from 0.2 ± 0.2 Pa/ μm at pulse minimum to 0.8 ± 0.6 Pa/ μm at pulse maximum. WSSG magnitudes in the parental vessels also increased as neck widths decreased. For example WSSG in the draining vessel at pulse max increased from 0.4 ± 0.3 Pa/ μm in AR 1.7 to 0.5 ± 0.4 Pa/ μm in AR 2.8 to 0.6 ± 0.5 Pa/ μm in AR 3.7.

WSSG was identified to increase from aneurysm sac to the parental vessels, for both feeding and draining vessels. Given the highly local gradients this leads to a very strong WSSG signal 0.5 Pa/ μm as compared to WSSG observed in-vitro 0.001 Pa/ μm (Dolan et al. 2011). Such large gradients in WSS were observed to cause endothelial cells to migrate toward the regions of maximum shear stress (Ostrowski et al. 2014).

3.1.1. Wall shear stress contribution of the red blood cells

The WSS and WSSG contribution by the individual RBCs is calculated by taking the difference in WSS

patterns in a time window of 0.001 second.

$$\tau_{cell} = |\tau_{i+1} - \tau_i| \quad (3)$$

This time window allows the differences in the WSS patterns on the vessel wall due to a passing cell to be captured. The patterns induced by a RBC are highlighted in Figure 5. In the left panel a single red blood cell is passing through the narrow constriction of the draining vessel of the original AR 2.8 geometry. The right panel shows the WSS pattern induced by a stiffened RBC, passing through the same constriction. The magnitude of WSSG is shown in the bottom row in Figure 5. Highlighted in this figure is the ability of the healthy red blood cell to deform and ‘squeeze’ through the narrow constriction of the parental vessel. The stiffened RBC however, cannot deform as easily and passes through in a relatively undeformed state. The stiffened RBCs, therefore, induce a larger WSS pattern onto the vessel wall.

The WSS patterns induced by passing cells are a highly local event. The RBC induced WSS signal is estimated in two ways. First by computing the spatial-temporal average of the WSS difference signal in the feeding and draining vessels. The spatial-temporal average allows for no distinction between single cell or multiple cell passing events and used to estimate the RBC WSS signal over a general vessel segment. RBC induced WSS is reported in Table 4. The mean RBC WSS in the AR 2.8 geometry is 0.5 ± 0.2 Pa feeding vessel and 0.9 ± 0.2 Pa for healthy RBCs. Stiffened

Table 4. Wall shear stress contribution of RBCs.

Geometry	Feeding vessel		Draining vessel	
	Mean WSS (Pa)	Max WSS (Pa)	Mean WSS (Pa)	Max WSS (Pa)
Healthy				
AR 1.7	0.08 ± 0.05	0.50 ± 0.04	0.10 ± 0.08	0.4 ± 0.2
AR 2.8	0.5 ± 0.2	0.9 ± 0.5	0.5 ± 0.2	0.7 ± 0.5
AR 3.7	0.5 ± 0.2	1.0 ± 0.5	0.5 ± 0.3	0.9 ± 0.6
Stiffened				
AR 2.8	0.7 ± 0.5	1.8 ± 1.2	0.6 ± 0.5	1.5 ± 1.2

RBCs were computed to induce a larger mean WSS signal with 0.7 ± 0.5 Pa in the feeding and 0.6 ± 0.5 Pa and draining vessels. The distribution of spatial-temporal RBC induced WSS values, for both parental vessels is shown in the middle left panel of Figure 4.

A more localized estimation for the RBC WSS signal is computed from the maximum WSS difference signal per cell passing event. The mean and standard deviation of the spatial-temporal maximum RBC induced WSS values is reported in Table 4 and the distribution of the values is shown in the bottom left panel of Figure 4. The maximum RBC WSS in the AR 2.8 geometry is 0.95 ± 0.52 Pa feeding vessel and 0.9 ± 0.6 Pa for healthy RBCs. Stiffened RBCs were computed to induce a markedly larger maximum WSS signal with 1.8 ± 1.2 Pa in the feeding and 1.5 ± 1.2 Pa in the draining vessels. Videos of the WSS patterns from the RBCs are included in the supplementary material.

Though the average values over the lifetime of the simulations are reported, some instances of WSS induced by passing RBCs were recorded as high as 1.66 Pa in the feeding vessel and 1.33 Pa in the draining vessel for healthy RBCs. The stiffened RBCs induced much higher WSS instances of 4.1 Pa in the leading and 3.76 Pa in the draining vessel. These values are comparable to previous cell resolved studies focusing on WSS patterns induced by single cell events in micro-vessels (Balogh and Bagchi 2019; Dabagh and Randles 2019).

The calculation of WSSG was carried out in the same as WSS. RBC induced WSSG, both mean and maximum, signals are reported in Table 5. The mean RBC WSSG in the AR 2.8 geometry is 0.03 ± 0.05 Pa/ μm feeding vessel and 0.015 ± 0.03 Pa/ μm for healthy RBCs. Stiffened RBCs were computed to induce a larger mean WSSG signal with 0.14 ± 0.12 Pa/ μm in the feeding and 0.12 ± 0.11 Pa/ μm and draining vessels. The maximum RBC WSSG in the AR 2.8 geometry is 0.32 ± 0.21 Pa/ μm feeding vessel and 0.14 ± 0.09 Pa/ μm for healthy RBCs. Stiffened RBCs were computed to induce a larger mean WSSG signal

Table 5. Wall shear stress gradient contribution of RBCs.

Geometry	Feeding vessel		Draining vessel	
	Mean WSSG (Pa/ μm)	Max WSSG (Pa/ μm)	Mean WSSG (Pa/ μm)	Max WSSG (Pa/ μm)
Healthy				
AR 1.7	0.001 ± 0.003	0.02 ± 0.02	0.009 ± 0.02	0.11 ± 0.08
AR 2.8	0.03 ± 0.05	0.32 ± 0.21	0.015 ± 0.03	0.14 ± 0.09
AR 3.7	0.03 ± 0.05	0.33 ± 0.22	0.024 ± 0.04	0.24 ± 0.18
Stiffened				
AR 2.8	0.14 ± 0.12	0.65 ± 0.42	0.12 ± 0.11	0.39 ± 0.25

with 0.65 ± 0.42 Pa/ μm in the feeding and 0.39 ± 0.25 Pa/ μm and draining vessels.

3.2. Cell volume fractions

3.2.1. Hematocrit

In order to quantify the difference in the spatial distribution of RBCs in healthy and stiffened cases, we compared the local hematocrit levels. Hematocrit was computed from each RBC Lagrangian surface point (LSP) location, and averaged over the entire simulation. Each RBC consists of 642 LSPs, subsequently each LSP was counted as 1/642th of the total volume of a RBC, which was $90 \mu\text{m}^3$. Average parental vessel hematocrit was computed to be 3.7% tube hematocrit, which was the initialized pre-inlet hematocrit. The cross section of the hematocrit differences across the pre-inlet is shown in Figure 6. Hematocrit differences are computed as the percent difference between local hematocrit values of healthy RBCs and stiffened RBCs. For each location in the aneurysm domain the hematocrit difference was calculated, i.e.

$$H_{diff} = \frac{H_{healthy} - H_{stiff}}{H_{Healthy}} \cdot 100 \quad (4)$$

Highlighted in Figure 6, is the difference in RBC cross sectional location in the pre-inlet. Locations where there were predominantly more healthy RBCs are shown in maroon and locations with more stiff RBCs are shown in pale blue. Here stiffened RBCs populate, on average, closer to the vessel wall compared to the healthy RBCs. This can be attributed to the fact that the stiffened cell experiences a lessened wall induced lift force when compared to the deformable healthy RBC. Since the stiffened RBC deforms less, therefore it has a lower reduced volume compared to the deformed RBC. A larger reduced volume has been found to influence the strength of the wall induced lift force on the RBC (Abkarian et al. 2002). The healthy RBC will also tank tread, which will further promote the lift force compared to a tumbling stiffened RBC (Olla 1997; Cantat and Misbah 1999; Abkarian et al. 2002). Pulsatility does not disrupt this

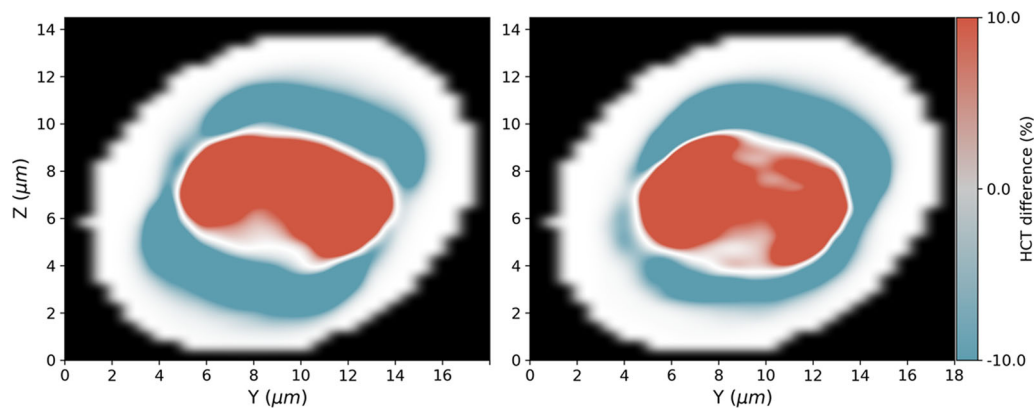


Figure 6. Healthy-stiff hematocrit differences cross sections in the pre-inlet. Hematocrit differences between stiffened and healthy RBCs in the cross-section of the pre-inlet domain. Steady state is shown in the left panel and pulsatile flow is shown in the right panel, values were averaged over the entire simulation (1 second).

effect, as the dominance of healthy RBCs in the vessel center is observed in both steady flow (left panel of Figure 6) and pulsatile flow (right panel of 6).

Side-view projections of hematocrit in each of the geometries are shown in Figure 7. Each column corresponds to a different geometry, the first two rows depict Hematocrit for healthy RBCs and stiff RBCs respectively, and the third row depicts positive and negative differences between healthy/stiff hematocrits. We observe over the entire simulation that cells do not significantly enter the aneurysm sac. This is consistent of both healthy and stiff RBC types and neck widths. Pulsatility has no significant effect on the penetration depth of both RBCs and platelets into the sac. Lower AR appears to increase the depth to which RBCs and platelets penetrate the sac, which is especially visible for AR 1.7. This can be attributed to a deeper penetration of the major streamlines from the parental vessel into the sac, in the AR 1.7 aneurysm. However, a velocity gradient still exists here, providing sufficient lift force to limit the penetration depth of the cells, lifting them out of the aneurysmal sac and into the draining vessel.

Stiffened RBCs are found to penetrate deeper into the aneurysm sac, shown in the bottom row of Figure 7. As stiffened RBCs enter the aneurysm, they are preferentially closer to the vessel wall, as observed in the pre-inlet, which will allow them to populate the slower streamlines and enter deeper into the aneurysm. They experience decreased lift out of the sac and into the draining vessel, further contributing to the deeper penetration.

3.2.2. Platelet volume fractions

Like the RBCs, platelets do not significantly penetrate the aneurysmal sac. They do however penetrate slightly more, because they are margined in the

parental vessel before entering the aneurysm. Since they are preferentially located closer to the vessel wall leading to the aneurysm, and therefore are more probable to enter deeper into the sac. This has previously been observed in 2D simulations of simple sidewall saccular/sacciform aneurysms (Czaja et al. 2018). The heatmaps show the difference of platelet volume fractions in stiffened and healthy RBC simulations, shown in Figure 8.

In the stiffened RBC case, platelet margination is decreased. Stiffened RBCs populate closer to the vessel wall, which decreases the red blood cell free layer and decreases the amount of platelets that are trapped in the CFL. Due to the low numbers and smaller size of the platelets, the resulting volume fraction heat maps exhibit a ‘spottier’ signal when compared to the RBC heatmaps. In order to alleviate this problem, higher temporal cell output is needed, to produce a smoother heatmap signal.

4. Summary

In this study we quantify the WSS patterns induced on a vessel wall of a segmented retinal microaneurysm through cell resolved blood flow simulations over a full second of pulsatile flow. We compute in the original segmented MA geometry that WSS in the feeding vessel has spatial-temporal average of 2.2 ± 1.7 Pa and in the draining vessel of 1.3 ± 1.1 Pa, with a significant drop in the aneurysm sac $(6.3 \pm 8.0) \times 10^{-4}$ Pa. The feeding vessel experiences higher WSS because it is narrower than the draining vessel. The computed spatial-temporal WSS means are in agreement with predictions made from in-vivo (Koutsiaris et al. 2007, 2013), in-vitro (DePaola et al. 1992; Tardy et al. 1997) and in-silico studies (Balogh and Bagchi 2019; Dabagh and Randles 2019; Hogan et al. 2019).

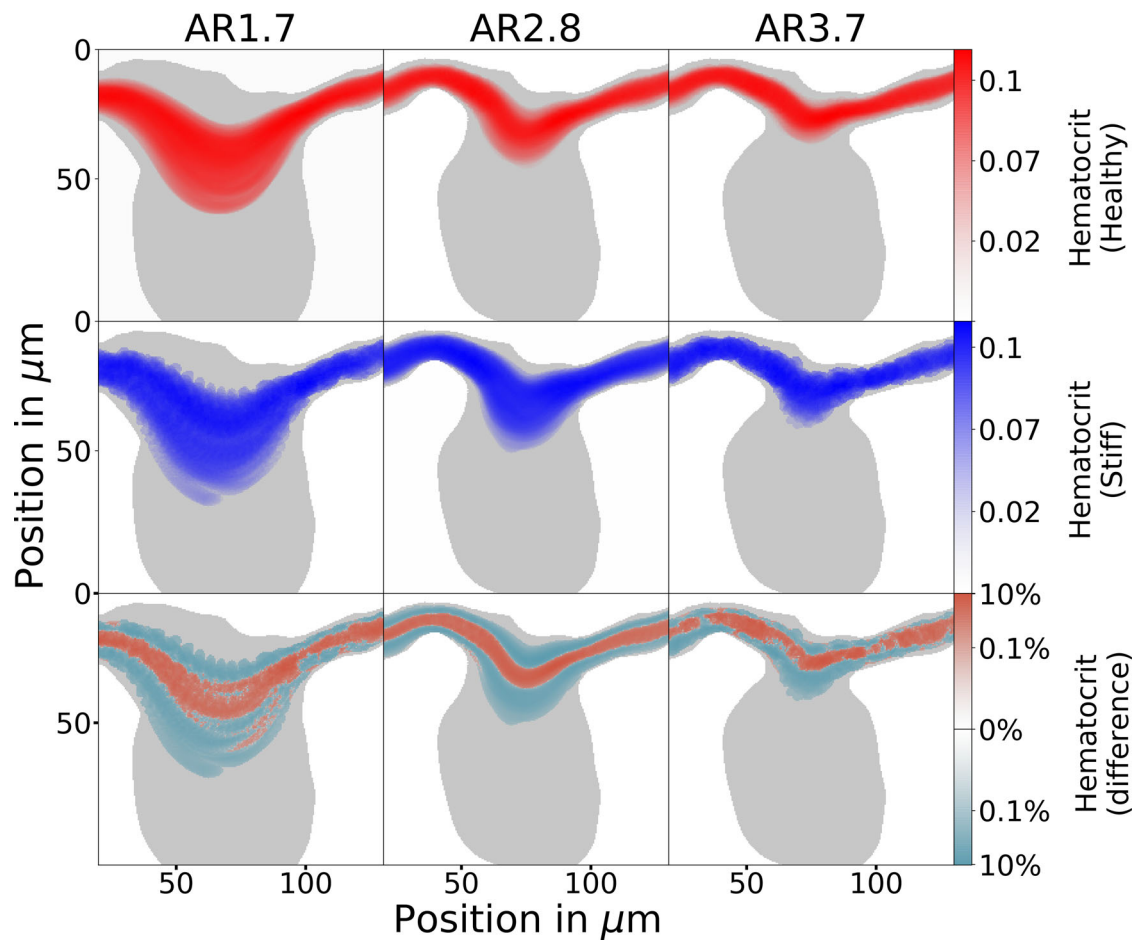


Figure 7. Time averaged side-view hematocrit heatmaps. The average volume fraction along the z-axis, i.e. the hematocrit, in red for healthy RBCs and in blue for stiff RBCs, vessel geometry is shown in gray. The third row shows the differences between the hematocrits from healthy/stiff simulations in maroon and pale blue. Each column corresponds to one of the three different geometries.

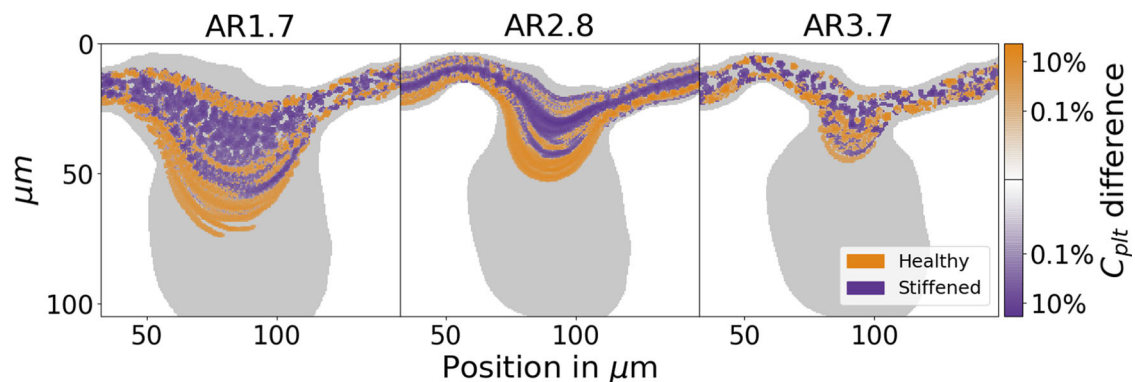


Figure 8. Average difference in platelet volume fractions. Shown here are the average difference in the platelet volume fractions in a healthy RBC simulation (orange) and a stiff RBC simulation (purple), projected onto the side-view of the aneurysm. Here, platelet volume fraction C_{plt} is reported as the fraction of the local radial platelet volume fraction C_{plt}^* to the mean vessel platelet volume fraction \bar{C}_{plt} . The percent difference is then $(C_{plt\text{healthy}} - C_{plt\text{stiffened}}) / (C_{plt\text{healthy}}) * 100$.

WSS in vessel diameters with similar sizes as the parental vessel considered in this study range have been estimated in-vivo to be between 0.5–3.0 Pa (Koutsiaris et al. 2007), and in-silico to be between 0.8–4.0 Pa (Balogh and Bagchi 2019). A significant finding from

this research is that pulsatility increases WSS in the parental vessels of the segmented microaneurysm from 0.9 ± 0.5 Pa at pulse minimum to 3.9 ± 2.2 Pa at pulse maximum. Pulsatile flow induces an approximate 3 Pa WSS signal change in the feeding and

draining vessels over an entire pulse. Non-invasive techniques have estimated WSS in the retina to be 5.4 Pa in the arterioles and 2.4 Pa in the venules (Nagaoka and Yoshida 2006), but relies on the assumption of a non-Newtonian continuous fluid solver to estimate the WSS from the measured velocity data. Additionally plasma-only simulations were carried out to highlight the difference when computing WSS with a continuous method in comparison to a cell based method. We show that the computed WSS is markedly higher in cell based simulations compared to continuous simulations. This highlights the importance of performing cellular resolved blood flow simulations at the microvascular scale.

Vascular endothelial growth factor is a protein that has been connected with diabetic retinopathy (Caldwell et al. 2003), specifically by inducing vessel permeability (Mathews et al. 1997) and the formation of new blood vessels (Aiello et al. 1995b; Hoeben et al. 2004). Elevated levels of VEGF have been measured in patients with proliferative DR (Adamis et al. 1994), and the expression of VEGF by the endothelial cells is stimulated by hemodynamic shear stresses on the vessel wall (Ballermann et al. 1998; Shay-Salit et al. 2002; Dela Paz et al. 2012). In-vitro work found that endothelial cells exposed to increased WSS (7.5 Pa) induced modifying gene expression and enhanced VEGF expression (White et al. 2011). Additionally the presence of spatial gradients in WSS have been identified in-vitro to influence endothelial cell proliferation and migration (DePaola et al. 1992; Tardy et al. 1997).

WSSG was identified in this study to increase from aneurysm sac to the parental vessels, for both feeding and draining vessels. Given the highly local computed WSSG, it is very strong ($0.5 \text{ Pa}/\mu\text{m}$) when compared to typical WSSG observed with in-vitro experiments ($0.001 \text{ Pa}/\mu\text{m}$) (Dolan et al. 2011; Ostrowski et al. 2014). It should be noted that the WSSG patterns computed in this study are over the spatial scale of 10 to $30 \mu\text{m}$, which are highly local compared to contemporary in-vitro studies. Highly localized WSSG over individual endothelial cells however has been suggested to transduce intra-cellular biochemical responses (Thi et al. 2004) that are important in endothelial cell shape, change, and alignment (Davies et al. 1995). Such large gradients in WSS were observed to cause endothelial cells to first proliferate in regions of high WSSG then migrate away (Ostrowski et al. 2014). In the context this study this would suggest that the WSSG magnitude increase toward the parental vessels from the aneurysm sac

would promote endothelial cell migration to the aneurysmal sac. Tracking the growth of an aneurysm over time, and subsequent cell resolved simulations carried out in different temporal morphologies of the same vessel can shed light on the evolution of aneurysm formation and the role that WSS and WSSG play.

The WSS from passing RBCs was also estimated in this study. RBCs on average were found to contribute $0.5 \pm 0.2 \text{ Pa}$ over the entire feeding vessel and $0.5 \pm 0.2 \text{ Pa}$ in draining vessel of the original MA. However RBCs can induce much higher local WSS as they pass through the vessel, which on average was computed to be $0.9 \pm 0.5 \text{ Pa}$ in the feeding vessel and $0.7 \pm 0.5 \text{ Pa}$ in the draining vessel. Balogh & Bagchi (Balogh and Bagchi 2019) identify that blood flow simulations including suspended RBCs in capillary networks significantly increased the computed WSS as compared to simulation without suspended RBCs. In this study the discharge hematocrit is 7% which is lower than the average physiological value of 10% (Klitzman and Duling 1979). This difference we anticipate can lead to a decrease in the computed WSS and WSSG signals in this study with respect to expected physiological values. In this study cell induced WSS and WSSG signals contribute to approximately 25% of the total WSS and WSSG signals over a full pulse wave. We anticipate that the magnitude of the cell induced WSS and WSSG will increase with increasing hematocrit because there will be more cell passing through the vessels per time.

Reactive oxygen species in diabetic patients has been found to increase the rigidity of the RBC membrane (Agrawal et al. 2016; Chang et al. 2017), which was incorporated in this study by increasing the RBC surface elastic modulus to $378.32 \frac{\mu\text{N}}{\text{m}}$. The increase of cell stiffness increased the spatial-temporal RBC induced WSS to $0.7 \pm 0.5 \text{ Pa}$ over the entire feeding vessel and $0.6 \pm 0.5 \text{ Pa}$ in draining vessel of the original MA. More locally stiffened RBCs were computed to produce higher maximum WSS as they pass through the vessel, which on average was computed to be $1.8 \pm 1.2 \text{ Pa}$ in the feeding vessel and $1.5 \pm 1.2 \text{ Pa}$ in the draining vessel. Though the results are focused on a time averaged WSS, occurrences of induced WSS from passing RBCs as high as 1.66 Pa in the healthy case and marked increase to 4.1 Pa in the stiffened case was observed. These maximum WSS signals depend on the number and orientation of cells traveling through the vessels. This increase in induced WSS as a result of increased cell stiffness has also been suggested through cell resolved simulations of

cancer cells passing through idealized geometries (Dabagh and Randles 2019).

Both RBCs and platelets do not significantly penetrate the aneurysmal sac for any of the variations of the neck widths, and is not significantly influenced by pulsatile flow. Larger aneurysm neck diameter (lower AR) increases the depth to which cells penetrate the aneurysm, which is highlighted by increased penetration of the blood plasma velocity streamlines into the aneurysmal sac for lower AR. These findings suggest an increase of intra-aneurysmal flow as neck width increases. A factor 100 mean drop in WSS was observed from the parental vessels to the aneurysmal sac, and such WSS mean drop increased as neck width decreased, which has been associated with an increased probability of forming a blood clot (Bernabeu et al. 2018). As WSS decreases in the aneurysm sac when neck width decreases cell penetration also decreases. Though it is not observed in this study the cell penetration findings can suggest that cells are more likely to be trapped in the sac as neck width decreases, therefore creating a more thrombogenic environment. Increasing amount of trapped cells with decreasing neck widths has been previously observed in 2D simulations of sidewall aneurysms (Czaja et al. 2018).

Stiffened RBCs undergo a reduction in deformability-dependent wall lift force (Olla 1997; Abkarian et al. 2002), which was observed as a decrease in the size of the cell-free layer in the parental vessel. This causes the stiffened RBCs to be on average closer to the vessel wall as they enter the aneurysmal sac more, as compared with healthy RBCs, allowing them to penetrate further into the sac. The deeper penetration of the stiffened RBCs is also promoted as they experience decreased lift out of the sac and into the draining vessel, compared to the healthy RBCs. The penetration of RBCs in to the body of microaneurysms thus appears to be a function of both inflow structure/shape, cell rigidity, and likely vessel permeability. Understanding how these factors interrelate may potentially explain, for example, why some microaneurysms are visible on Optical Coherence Tomography Angiography while others are not. Platelet margination is also effected by the presence of stiffened RBCs in flow, since the stiffened RBCs reduce the cell free layer, therefore reducing the probability of a platelet becoming trapped in the cell free layer. This decrease of platelet concentration at the wall, leads to a decreased penetration of platelets into the aneurysmal sac, when RBCs are stiffened. Platelet margination has been shown to depend on cell size

and shape (Fedosov et al. 2012), as well as deformability of the RBCs (Zhao and Shaqfeh 2011), which also crucially depends on hematocrit. A decrease in platelet margination has been observed in systems with increasing amounts of stiffened RBCs present in flow (Czaja et al. 2020).

Initializing the domain cell volume fractions is a limiting factor in this study. Reaching an equilibrium aneurysmal sac hematocrit has been estimated to require >25 seconds of simulation (Czaja et al. 2018) in a larger cerebral aneurysm like domain. Though this may require shorter timescales for smaller aneurysms like MAs, we estimate that equilibrium hematocrit will likely occur after many physical seconds, which is above the reasonable timescales currently simulated by 3D cell resolved blood flow solvers. Uniformly initializing the entire domain is also problematic, as the assumed cell distributions can impact the final computed hematocrit profiles. Future work of this kind can investigate the flow and transport of blood cells into a MA when the domain is initialized filled with cells.

Differences in parental vessel diameters in this study were not considered as the computational overhead significantly limited a parametric study of vessel morphology. As observational techniques improve this may open up morphological cell resolved studies as smaller aneurysms could be reliably segmented, and therefore less expensive to simulate. Future work could also incorporate the increased vessel permeability that is characteristic of diabetic retinopathy (Mathews et al. 1997; Ciulla et al. 2003). Since flow in MA is substantially slower flow (Reynolds numbers < 0.1), compared to larger aneurysms in the body, it is unlikely that secondary intra-aneurysmal flow can develop as it does in the larger, faster flow, that exists in cerebral aneurysms (Cebal et al. 2004). Including vessel boundary conditions that model vessel permeability may lead to incite on the sensitivity of the flow environment, and could therefore promote transport of blood cells into sidewall sacciform MAs such as the geometry considered in this study.

Acknowledgments

We would like to thank Dr. Miguel Bernabeu from the University of Edinburgh for the initial inspiration, and early conversations regarding numerical simulations in microaneurysm.

Disclosure statement

The authors declare that no competing interests exist and the funding organizations had no role in study design, data

collection and analysis, decision to publish, or preparation of the manuscript.

Funding

This work was supported by the European Union Horizon 2020 research and innovation programme under Grant Agreement No. 675451 (phase 1 CompBioMed project) and grant agreement No. 823712 (phase 2 CompBioMed project). This work was sponsored by NWO Exacte Wetenschappen (Physical Sciences) for the use of super-computer facilities, with financial support from the Nederlandse Organisatie voor Wetenschappelijk Onderzoek (Netherlands Organization for Science Research, NWO).

References

- Abkarian M, Lartigue C, Viallat A. 2002. Tank treading and unbinding of deformable vesicles in shear flow: determination of the lift force. *Phys Rev Lett.* 88(6):068103.
- Adamis AP, Miller JW, Bernal M-T, D'Amico DJ, Folkman J, Yeo T-K, Yeo K-T. 1994. Increased vascular endothelial growth factor levels in the vitreous of eyes with proliferative diabetic retinopathy. *Am J Ophthalmol.* 118(4):445–450.
- Agrawal R, Smart T, Nobre-Cardoso J, Richards C, Bhatnagar R, Tufail A, Shima D, Jones PH, Pavesio C. 2016. Assessment of red blood cell deformability in type 2 diabetes mellitus and diabetic retinopathy by dual optical tweezers stretching technique. *Sci Rep.* 6(1):15873.
- Ahsan H. 2015. Diabetic retinopathy-biomolecules and multiple pathophysiology. *Diabetes Metab Syndr.* 9(1):51–54.
- Aiello LP, Avery RL, Arrigg PG, Keyt BA, Jampel HD, Shah ST, Pasquale LR, Thieme H, Iwamoto MA, Park JE, et al. 1994. Vascular endothelial growth factor in ocular fluid of patients with diabetic retinopathy and other retinal disorders. *N Engl J Med.* 331(22):1480–1487.
- Aiello LP, Northrup JM, Keyt BA, Takagi H, Iwamoto MA. 1995a. Hypoxic regulation of vascular endothelial growth factor in retinal cells. *Arch Ophthalmol.* 113(12):1538–1544.
- Aiello LP, Pierce EA, Foley ED, Takagi H, Chen H, Riddle L, Ferrara N, King GL, Smith L. 1995b. Suppression of retinal neovascularization in vivo by inhibition of vascular endothelial growth factor (VEGF) using soluble VEGF-receptor chimeric proteins. *Proc Natl Acad Sci.* 92(23):10457–10461.
- Azizi Tarksalooyeh VW, Závodszy G, J. M. van Rooij B, Hoekstra AG. 2018. Inflow and outflow boundary conditions for 2D suspension simulations with the immersed boundary lattice Boltzmann method. *Comput Fluids.* 172:312–317.
- Bagchi P. 2007. Mesoscale simulation of blood flow in small vessels. *Biophys J.* 92(6):1858–1877.
- Ballermann BJ, Dardik A, Eng E, Liu A. 1998. Shear stress and the endothelium. *Kidney Int.* 54:S100–S108.
- Balogh P, Bagchi P. 2019. Three-dimensional distribution of wall shear stress and its gradient in red cell-resolved computational modeling of blood flow in in vivo-like microvascular networks. *Physiol Rep.* 7(9):e14067.
- Bargiel M, Mościński J. 1991. C-language program for the irregular close packing of hard spheres. *Comput Phys Commun.* 64(1):183–192.
- Bernabeu MO, Lu Y, Abu-Qamar O, Aiello LP, Sun JK. 2018. Estimation of diabetic retinal microaneurysm perfusion parameters based on computational fluid dynamics modeling of adaptive optics scanning laser ophthalmoscopy. *Front Physiol.* 9(989).
- Bhogal P, AlMatter M, Hellstern V, Ganslandt O, Bätzner H, Henkes H, Pérez MA. 2018. Difference in aneurysm characteristics between ruptured and unruptured aneurysms in patients with multiple intracranial aneurysms. *Surg Neurol Int.* 9(1):1.
- Bird RB, Stewart WE, Lightfoot EN. 2007. Transport phenomena. Hoboken, NJ: John Wiley & Sons.
- Caldwell RB, Bartoli M, Behzadian MA, El-Remessy AE, Al-Shabrawey M, Platt DH, Caldwell RW. 2003. Vascular endothelial growth factor and diabetic retinopathy: pathophysiological mechanisms and treatment perspectives. *Diabetes Metab Res Rev.* 19(6):442–455.
- Cantat I, Misbah C. 1999. Lift force and dynamical unbinding of adhering vesicles under shear flow. *Phys Rev Lett.* 83(4):880–883.
- Caprari P, Bozzi A, Malorni W, Bottini A, Iosi F, Santini MT, Salvati AM. 1995. Junctional sites of erythrocyte skeletal proteins are specific targets of tert-butylhydroperoxide oxidative damage. *Chem Biol Interact.* 94(3):243–258.
- Care D, et al. 2006. Diagnosis and classification of diabetes mellitus. *Diabetes Care.* 28(S37):S5–S10.
- Cebral JR, Hernandez M, Frangi A, Putman C, Pergolizzi R, Burgess J. 2004. Subject-specific modeling of intracranial aneurysms. In *Medical imaging 2004: physiology, function, and structure from medical images.* Vol. 5369. San Diego, CA: International Society for Optics and Photonics. p. 319–327.
- Chang H-Y, Li X, Karniadakis GE. 2017. Modeling of biomechanics and biorheology of red blood cells in type 2 diabetes mellitus. *Biophys J.* 113(2):481–490.
- Ciulla TA, Amador AG, Zinman B. 2003. Diabetic retinopathy and diabetic macular edema: pathophysiology, screening, and novel therapies. *Diabetes Care.* 26(9):2653–2664.
- Czaja B, Gutierrez M, Závodszy G, de Kanter D, Hoekstra A, Eniola-Adefeso O. 2020. The influence of red blood cell deformability on hematocrit profiles and platelet margination. *PLOS Comput Biol.* 16(3):e1007716.
- Czaja B, Závodszy G, Azizi Tarksalooyeh V, Hoekstra A. 2018. Cell-resolved blood flow simulations of saccular aneurysms: effects of pulsatility and aspect ratio. *J R Soc Interface.* 15(146):20180485.
- Dabagh M, Randles A. 2019. Role of deformable cancer cells on wall shear stress-associated-VEGF secretion by endothelium in microvasculature. *PLoS One.* 14(2):e0211418.
- Davies PF, Mundel T, Barbee KA. 1995. A mechanism for heterogeneous endothelial responses to flow in vivo and in vitro. *J Biomech.* 28(12):1553–1560.
- de Castro A, Huang G, Sawides L, Luo T, Burns SA. 2016. Rapid high resolution imaging with a dual-channel scanning technique. *Opt Lett.* 41(8):1881.
- De Haan M, Zavodszy G, Azizi V, Hoekstra AG. 2018. Numerical investigation of the effects of red blood cell

- cytoplasmic viscosity contrasts on single cell and bulk transport behaviour. *Appl Sci.* 8(9):1616.
- de Sousa DR, Vallecilla C, Chodzynski K, Jerez RC, Malaspinas O, Eker OF, Ouared R, Vanhamme L, Legrand A, Chopard B, et al. 2016. Determination of a shear rate threshold for thrombus formation in intracranial aneurysms. *J NeuroIntervent Surg.* 8(8):853–858.
- de Vries K, Nikishova A, Czaja B, Závodszy G, Hoekstra AG. 2020. Inverse uncertainty quantification of a cell model using a gaussian process metamodel. *Int J Uncertainty Quantification.* 10(4):333–349.
- Dela Paz NG, Walshe TE, Leach LL, Saint-Geniez M, D'Amore PA. 2012. Role of shear-stress-induced vegf expression in endothelial cell survival. *J Cell Sci.* 125(Pt 4):831–843.
- DePaola N, Gimbrone MA, Jr, Davies PF, Dewey Jr CF. 1992. Vascular endothelium responds to fluid shear stress gradients. *Arterioscler Thromb.* 12(11):1254–1257.
- Dolan JM, Meng H, Singh S, Paluch R, Kolega J. 2011. High fluid shear stress and spatial shear stress gradients affect endothelial proliferation, survival, and alignment. *Ann Biomed Eng.* 39(6):1620–1631.
- Dubov M, Pinhas A, Shah N, Cooper RF, Gan A, Gentile RC, Hendrix V, Sulai YN, Carroll J, Chui TY, et al. 2014. Classification of human retinal microaneurysms using adaptive optics scanning light ophthalmoscope fluorescein angiography. *Invest Ophthalmol Vis Sci.* 55(3):1299–1309.
- Engerman R. 1996. The pathogenesis of diabetic retinopathy. *Australian and New Zealand Journal of Ophthalmology.* 24(2):97–104.
- Evans EA. 1983. Bending elastic modulus of red blood cell membrane derived from buckling instability in micropipet aspiration tests. *Biophys J.* 43(1):27–30.
- Ezra E, Keinan E, Mandel Y, Boulton ME, Nahmias Y. 2013. Non-dimensional analysis of retinal microaneurysms: critical threshold for treatment. *Integr Biol (Camb).* 5(3):474–480.
- Fåhræus R, Lindqvist T. 1931. The viscosity of the blood in narrow capillary tubes. *Am J Physiol-Legacy Content.* 96(3):562–568.
- Faust O, Acharya UR, Ng EYK, Ng K-H, Suri JS. 2012. Algorithms for the automated detection of diabetic retinopathy using digital fundus images: a review. *J Med Syst.* 36(1):145–157.
- Fedosov DA, Caswell B, Karniadakis GE. 2010. A multiscale red blood cell model with accurate mechanics, rheology, and dynamics. *Biophys J.* 98(10):2215–2225.
- Fedosov DA, Fornleitner J, Gompper G. 2012. Margination of white blood cells in microcapillary flow. *Phys Rev Lett.* 108(2):028104.
- Fong DS, Blankenship G, Klein R, King GL, Gardner TW, Cavallerano JD, Aiello L, Ferris FL. 2007. Retinopathy in diabetes. Technical Report Supplement 1, American Diabetes Association.
- Garnier M, Attali JR, Valensi P, Delatour-Hanss E, Gaudoy F, Koutsouris D. 1990. Erythrocyte deformability in diabetes and erythrocyte membrane lipid composition. *Metabolism.* 39(8):794–798.
- Giugliano D, Ceriello A, Paolisso G. 1996. Oxidative stress and diabetic vascular complications. *Diabetes Care.* 19(3):257–267.
- Gu B, Wang X, Twa MD, Tam J, Girkin CA, Zhang Y. 2018. Noninvasive in vivo characterization of erythrocyte motion in human retinal capillaries using high-speed adaptive optics near-confocal imaging. *Biomed Opt Express.* 9(8):3653.
- Gupta N, Mansoor S, Sharma A, Sapkal A, Sheth J, Falatoonzadeh P, Kuppermann B, Kenney M. 2013. Diabetic retinopathy and vegf. *Open Ophthalmol J.* 7(4):10.
- Haga JH, Beaudoin AJ, White JG, Strony J. 1998. Quantification of the passive mechanical properties of the resting platelet. *Ann Biomed Eng.* 26(2):268–277.
- Heisler M, Ju MJ, Bhalla M, Schuck N, Athwal A, Navajas EV, Beg MF, Sarunic MV. 2018. Automated identification of cone photoreceptors in adaptive optics optical coherence tomography images using transfer learning. *Biomed Opt Express.* 9(11):5353–5367.
- Hennis A, Wu S-Y, Nemesure B, Leske MC, Group BES. 2003. Hypertension, diabetes, and longitudinal changes in intraocular pressure. *Ophthalmology.* 110(5):908–914.
- Hoeben A, Landuyt B, Highley MS, Wildiers H, Van Oosterom AT, De Bruijn EA. 2004. Vascular endothelial growth factor and angiogenesis. *Pharmacol Rev.* 56(4):549–580.
- Hogan B, Shen Z, Zhang H, Misbah C, Barakat AI. 2019. Shear stress in the microvasculature: influence of red blood cell morphology and endothelial wall undulation. *Biomech Model Mechanobiol.* 18(4):1095–1109.
- Hoskins PR, Hardman D. 2017. Blood and blood flow. Switzerland: Springer.
- Johnson PC. 1971. Red cell separation in the mesenteric capillary network. *Am J Physiol.* 221(1):99–104.
- Ju MJ, Heisler M, Wahl D, Jian Y, Sarunic MV. 2017. Multiscale sensorless adaptive optics OCT angiography system for in vivo human retinal imaging. *J Biomed Opt.* 22(12):1.
- Karst SG, Lammer J, Radwan SH, Kwak H, Silva PS, Burns SA, Aiello LP, Sun JK. 2018. Characterization of in vivo retinal lesions of diabetic retinopathy using adaptive optics scanning laser ophthalmoscopy. *Int J Endocrinol.* 2018:7492946.
- Katanov D, Gompper G, Fedosov DA. 2015. Microvascular blood flow resistance: role of red blood cell migration and dispersion. *Microvasc Res.* 99:57–66.
- Kempner JH, O'Colmain BJ, Leske MC, Haffner SM, Klein R, Moss SE, Taylor HR, Hamman RF. 2004. The prevalence of diabetic retinopathy among adults in the United States. *Arch Ophthalmol.* 122(4):552–563.
- Klein R, Klein BEK. 2002. Blood pressure control and diabetic retinopathy. *Br J Ophthalmol.* 86(4):365–367.
- Klitzman B, Duling BR. 1979. Microvascular hematocrit and red cell flow in resting and contracting striated muscle. *Am J Physiol-Heart Circ Physiol.* 237(4):H481–H490.
- Kohner E. 1993. The retinal blood flow in diabetes. *Diabetes Metab.* 19(5):401–404.
- Kotsalos C, Latt J, Chopard B. 2019. Bridging the computational gap between mesoscopic and continuum modeling of red blood cells for fully resolved blood flow. *Comput Phys.* 398:108905.
- Koutsouris AG, Tachmitzi SV, Batis N. 2013. Wall shear stress quantification in the human conjunctival pre-capillary arterioles in vivo. *Microvasc Res.* 85:34–39.

- Koutsiaris AG, Tachmitzi SV, Batis N, Kotoula MG, Karabatsas CH, Tsironi E, Chatzoulis DZ. 2007. Volume flow and wall shear stress quantification in the human conjunctival capillaries and post-capillary venules in vivo. *Biorheology*. 44(5–6):375–386.
- Krüger T, Varnik F, Raabe D. 2009. Shear stress in lattice Boltzmann simulations. *Phys Rev E Stat Nonlin Soft Matter Phys*. 79(4 Pt 2):046704.
- Lammer J, Karst SG, Lin MM, Cheney M, Silva PS, Burns SA, Aiello LP, Sun JK. 2018. Association of microaneurysms on adaptive optics scanning laser ophthalmoscopy with surrounding neuroretinal pathology and visual function in diabetes. *Invest Ophthalmol Vis Sci*. 59(13):5633–5640.
- Lipowsky HH, Kovalcheck S, Zweifach BW. 1978. The distribution of blood rheological parameters in the microvasculature of cat mesentery. *Circ Res*. 43(5):738–749.
- Lombardo M, Parravano M, Serrao S, Ducoli P, Stirpe M, Lombardo G. 2013. Analysis of retinal capillaries in patients with type 1 diabetes and nonproliferative diabetic retinopathy using adaptive optics imaging. *Retina*. 33(8):1630–1639.
- Lu Y, Bernabeu MO, Lammer J, Cai CC, Jones ML, Franco CA, Aiello LP, Sun JK. 2016. Computational fluid dynamics assisted characterization of parafoveal hemodynamics in normal and diabetic eyes using adaptive optics scanning laser ophthalmoscopy. *Biomed Opt Express*. 7(12):4958–4973.
- Maciaszek JL, Lykotrafitis G. 2011. Sickle cell trait human erythrocytes are significantly stiffer than normal. *J Biomech*. 44(4):657–661.
- Maner BS, Moosavi L. 2019. Mean corpuscular volume.
- Mathews MK, Merges C, McLeod DS, Luty GA. 1997. Vascular endothelial growth factor and vascular permeability changes in human diabetic retinopathy. *Invest Ophthalmol Vis Sci*. 38(13):2729–2741.
- McWhirter JL, Noguchi H, Gompper G. 2009. Flow-induced clustering and alignment of vesicles and red blood cells in microcapillaries. *Proc Natl Acad Sci U S A*. 106(15):6039–6043.
- Melchionna S, Bernaschi M, Succi S, Kaxiras E, Rybicki FJ, Mitsouras D, Coskun AU, Feldman CL. 2010. Hydrokinetic approach to large-scale cardiovascular blood flow. *Comput Phys Commun*. 181(3):462–472.
- Meng H, Tutino VM, Xiang J, Siddiqui A. 2014. High WSS or Low WSS? Complex interactions of hemodynamics with intracranial aneurysm initiation, growth, and rupture: toward a unifying hypothesis. *Ajnr Am J Neuroradiol*. 35(7):1254–1262.
- Moore J, Bagley S, Ireland G, McLeod D, Boulton M. 1999. Three dimensional analysis of microaneurysms in the human diabetic retina. *J Anatomy*. 194(1):89–100.
- Mountrakis L, Lorenz E, Hoekstra A. 2013. Where do the platelets go? A simulation study of fully resolved blood flow through aneurysmal vessels. *Interface Focus*. 3(2):20120089.
- Nagaoka T, Yoshida A. 2006. Noninvasive evaluation of wall shear stress on retinal microcirculation in humans. *Invest Ophthalmol Vis Sci*. 47(3):1113–1119.
- Noguchi H, Gompper G. 2005. Shape transitions of fluid vesicles and red blood cells in capillary flows. *Proc Natl Acad Sci USA*. 102(40):14159–14164.
- Ogurtsova K, da Rocha Fernandes JD, Huang Y, Linnenkamp U, Guariguata L, Cho NH, Cavan D, Shaw JE, Makaroff LE. 2017. IDF Diabetes Atlas: global estimates for the prevalence of diabetes for 2015 and 2040. *Diabetes Res Clin Pract*. 128:40–50.
- Olla P. 1997. The lift on a tank-treading ellipsoidal cell in a shear flow. *J Phys II France*. 7(10):1533–1540.
- Ostrowski MA, Huang NF, Walker TW, Verwijlen T, Poplawski C, Khoo AS, Cooke JP, Fuller GG, Dunn AR. 2014. Microvascular endothelial cells migrate upstream and align against the shear stress field created by impinging flow. *Biophys J*. 106(2):366–374.
- Park Y, Best CA, Kuriabova T, Henle ML, Feld MS, Levine AJ, Popescu G. 2011. Measurement of the nonlinear elasticity of red blood cell membranes. *Phys Rev E*. 83(5):051925.
- Pries A, Secomb T, Gessner T, Sperandio M, Gross J, Gaehtgens P. 1994. Resistance to blood flow in microvessels in vivo. *Circ Res*. 75(5):904–915.
- Rooij BJMV, Závodszy G, Tarksalooeyh VWA, Hoekstra AG. 2019. Identifying the start of a platelet aggregate by the shear rate and the cell-depleted layer. *J R Soc Interface*. 16(159):20190148.
- Roy S, Ha J, Trudeau K, Beglova E. 2010. Vascular basement membrane thickening in diabetic retinopathy. *Curr Eye Res*. 35(12):1045–1056.
- Sampani K, Abu-Qamar O, Raval N, Lu Y, Bernabeu MO, Fickweiler W, Aiello LP, Sun JK. 2018. Optical Coherence Tomography Angiography (OCTA) Visibility of Diabetic Microaneurysms (MAs): associations with wall characteristics and blood flow parameters. The New England Ophthalmological Society Meeting.
- Sforza DM, Putman CM, Cebra JR. 2009. Hemodynamics of cerebral aneurysms. *Annu Rev Fluid Mech*. 41:91–107.
- Sforza DM, Putman CM, Cebra JR. 2012. Computational fluid dynamics in brain aneurysms. *Int J Numer Method Biomed Eng*. 28(6–7):801–808.
- Shay-Salit A, Shushy M, Wolfowitz E, Yahav H, Breviaro F, Dejana E, Resnick N. 2002. VEGF receptor 2 and the adherens junction as a mechanical transducer in vascular endothelial cells. *Proc Natl Acad Sci USA*. 99(14):9462–9467.
- Shin S, Ku Y-H, Ho J-X, Kim Y-K, Suh J-S, Singh M. 2007. Progressive impairment of erythrocyte deformability as indicator of microangiopathy in type 2 diabetes mellitus. *Clin Hemorheol Microcirc*. 36(3):253–261.
- Stahl B, Chopard B, Latt J. 2010. Measurements of wall shear stress with the lattice Boltzmann method and staircase approximation of boundaries. *Comput Fluids*. 39(9):1625–1633.
- Tardy Y, Resnick N, Nagel T, Gimbrone M, Jr, Dewey Jr C. 1997. Shear stress gradients remodel endothelial monolayers in vitro via a cell proliferation-migration-loss cycle. *Arterioscler Thromb Vasc Biol*. 17(11):3102–3106.
- Tarr JM, Kaul K, Chopra M, Kohner ME, Chibber R. 2010. Pathophysiology of diabetic retinopathy. In *Diabetic retinopathy: evidence-based management*. Vol. 2013. p. 1–30. UK: ISRN Ophthalmology.
- Thi MM, Tarbell JM, Weinbaum S, Spray DC. 2004. The role of the glycocalyx in reorganization of the actin cytoskeleton under fluid shear stress: a ‘bumper-car’ model. *Proc Natl Acad Sci U S A*. 101(47):16483–16488.

- Timm K, Kusumaatmaja H, Kuzmin A. 2016. The lattice Boltzmann method: principles and practice.
- Tsukada K, Sekizuka E, Oshio C, Minamitani H. 2001. Direct measurement of erythrocyte deformability in diabetes mellitus with a transparent microchannel capillary model and high-speed video camera system. *Microvasc Res.* 61(3):231–239.
- Ujii H, Tamano Y, Sasaki K, Hori T. 2001. Is the aspect ratio a reliable index for predicting the rupture of a saccular aneurysm? *Neurosurgery.* 48(3):495–503.
- White SJ, Hayes EM, Lehoux S, Jeremy JY, Horrevoets AJ, Newby AC. 2011. Characterization of the differential response of endothelial cells exposed to normal and elevated laminar shear stress. *J Cell Physiol.* 226(11):2841–2848.
- Wilkinson C, Ferris III, Klein FL, Lee RE, Agardh PP, Davis CD, Dills M, Kampik D, Pararajasegaram A, Verdaguer R, et al. 2003. Proposed international clinical diabetic retinopathy and diabetic macular edema disease severity scales. *Ophthalmology.* 110(9):1677–1682.
- Williams R, Airey M, Baxter H, Forrester J, Kennedy-Martin T, Girach A. 2004. Epidemiology of diabetic retinopathy and macular oedema: a systematic review. *Eye (Lond).* 18(10):963–983.
- Závodszy G, van Rooij B, Azizi V, Hoekstra A. 2017. Cellular level in-silico modeling of blood rheology with an improved material model for red blood cells. *Front Physiol.* 8(563).
- Závodszy G, van Rooij B, Czaja B, Azizi V, de Kanter D, Hoekstra AG. 2019. Red blood cell and platelet diffusivity and margination in the presence of cross-stream gradients in blood flows. *Phys. Fluids.* 31(3):031903.
- Zhao H, Shaqfeh ES. 2011. Shear-induced platelet margination in a microchannel. *Phys Rev E.* 83(6):061924.